

Domain wall motion in magnetically frustrated nanorings

M. V. Lubarda, M. A. Escobar, S. Li, R. Chang, E. E. Fullerton, and V. Lomakin

Center for Magnetic Recording Research, Department of Electrical and Computer Engineering, University of California, San Diego, California 92093, USA

(Received 22 February 2012; published 25 June 2012)

We describe a magnetically frustrated nanoring (MFNR) configuration which is formed by introducing antiferromagnetic coupling across an interface orthogonal to the ring's circumferential direction. Such structures have the unique characteristic that only one itinerant domain wall (DW) can exist in the ring, which does not need to be nucleated or injected into the structure and can never escape making it analogous to a magnetic Möbius strip. Numerical simulations show that the DW in a MFNR can be driven consecutively around the ring with a prescribed cyclicity, and that the frequency of revolutions can be controlled by the applied field. The energy landscapes can be controlled to be flat allowing for low fields of operation or to have a barrier for thermal stability. Potential logic and memory applications of MFNRs are considered and discussed.

DOI: [10.1103/PhysRevB.85.214428](https://doi.org/10.1103/PhysRevB.85.214428)

PACS number(s): 75.78.Fg, 75.60.Ch, 75.78.Cd, 85.70.-w

I. INTRODUCTION

Magnetic nanoring structures have been the focus of recent research interest due to their attractiveness for technological applications such as nonvolatile solid-state memory and magnetic logic circuits.¹⁻³ Due to their topological characteristics magnetic nanorings can exhibit multiple stable remanent states, controlled by external magnetic fields or currents.¹⁻⁷ Logic gates have also been engineered to perform Boolean operations such as NOT and AND using all-magnetic loop architectures.⁸⁻¹⁰ In this paper we model magnetically frustrated nanorings (MFNRs) and describe their magnetic properties, with particular attention to energy landscapes and domain wall (DW) motion.

Magnetic frustration implies a competition between different energy terms so that an energy minimization in one area involves an increase of energy in another. Magnetic frustration is often seen in coupled multilayer systems, due to interfacial disorder¹¹ or the competition between lateral and vertical exchange.¹² In antiferromagnetic materials, it can occur due to the lattice topology, which can prevent all spins from being antiferromagnetically paired.¹³ Molecular structures including flakes and ring chains have been seen to exhibit geometrically induced frustration as well.¹⁴ Magnetic frustration in MFNR presented here is achieved by introducing antiferromagnetic (AF) coupling across an interface orthogonal to the circumferential direction of the ring as illustrated in Fig. 1. As a consequence of such a configuration, the remanent state of the ring involves a DW with an associated DW energy. This is the case regardless of the dominant form of anisotropy (shape or magnetocrystalline). A similar effect would be achieved in a magnetic Möbius strip with a half turn.

For the ring in Fig. 1 we have chosen perpendicular magnetocrystalline anisotropy (PMA), so that the magnetization tends toward a vertical orientation. In Fig. 1(a) the magnetization changes orientation twice along the ring, once at the interface at point *A* due to the AF coupling, and again at some point *B* in the ring, as a result of system topology. It is important to distinguish between the magnetization reorientation at point *A* and point *B*, because in the former case there is no energy stored in the DW. Only the magnetization reorientation at point *B* constitutes a DW in the usual sense,

with an associated DW energy and mobility. Therefore, the system is fundamentally different from a simple continuous nanoring, as a single DW persists in the system at remanence.⁹ By tuning the system parameters, the energy landscape can be made nearly flat, as will be shown below. As a result, the DW can be driven by a weak field and can reside at any location along the MFNR, including the AF interface [Figs. 1(b) and 2]. Since the system is characterized by a single mobile DW, with an associated DW energy, there is no concern that two DWs may converge and annihilate. The DW can move in any direction, e.g., it can make multiple complete revolutions around the ring with a specified cyclicity, driven by an applied field. Furthermore, the AF interface eliminates the need for strict synchronization between the external stimulus and DW propagation time due to a tunable DW dwell time at the interface, as shown below.

II. ENERGY CALCULATIONS

To calculate the energy we use the nudged elastic band method approach (see the Appendix).¹⁵ The particular choice of simulation parameters chosen here was to demonstrate the energy landscapes and DW motion in a PMA nanoring. Other parameter values can be used for realization of both perpendicular and in-plane MFNRs. Depending on the strength of AF coupling J_{AF} at the interface, there will be extrema and saddle points in the energy landscape. Figure 3(a) shows that the energy landscape of the nanoring can be tailored by modulating J_{AF} at the AF interface. As $|J_{AF}|$ is reduced, the energy of the system when the DW is at the AF interface [Fig. 1(b)] significantly decreases. When $|J_{AF}|$ is increased, the energetic favorability of the DW to reside at the AF interface disappears as the cost of overcoming the AF coupling energy increases. For appropriate parameters, the MFNR can be tailored so that the energy of the system is nearly independent of the position of the DW along the ring [see the red curve with point markers in Fig. 3(a)]. The DW can lie away from the AF interface, as in Fig. 1(a), or at the AF interface, as in Fig. 1(b), with the system energy equal in both cases.

Figure 2(a) shows the DW configuration near and at the AF interface. The DW structure away and at the interface can be very different without a significant difference in energy

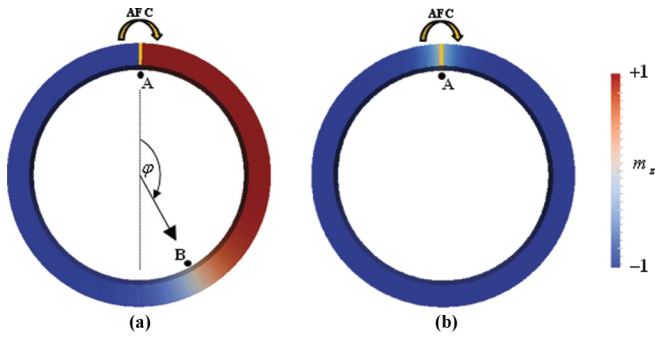


FIG. 1. (Color online) Perpendicular magnetic anisotropy nanoring with AF coupling across interface (colored yellow) located at point A. Due to the magnetic frustration introduced by the AF coupling only one mobile DW with an associated nonzero DW energy can exist. The DW can reside either away [Fig. 1(a), point B] or at the AF interface [Fig. 1(b), point A].

[material and structural parameters used for the MFNR in Fig. 2(a) are the same as those used for the MFNR leading to the black curve (diamond plot markers) in Fig. 3(a)]. It can be seen that, when the DW is at the interface [Fig. 2(a)], the magnetization is largely antiparallel, as expected for AF coupling, with an alignment orthogonal to the ring’s circumferential direction, corresponding to a magnetostatically favorable

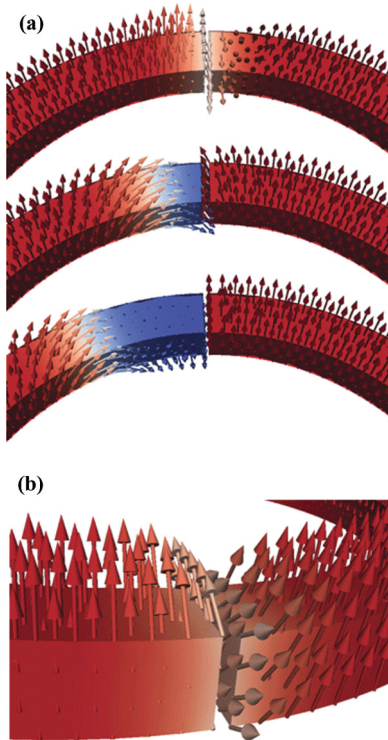


FIG. 2. (Color online) DW configurations near and at the AF interface for (a) relatively strong and (b) weak AF exchange coupling. When AF coupling is large in comparison to the perpendicular anisotropy energy, the DW at the AF interface shows an antiparallel head-to-tail configuration with the DW magnetization largely along the in-plane direction (a). For reduced AF coupling, the perpendicular magnetocrystalline anisotropy tilts the magnetization vertically at the expense of the antiparallel configuration (b).

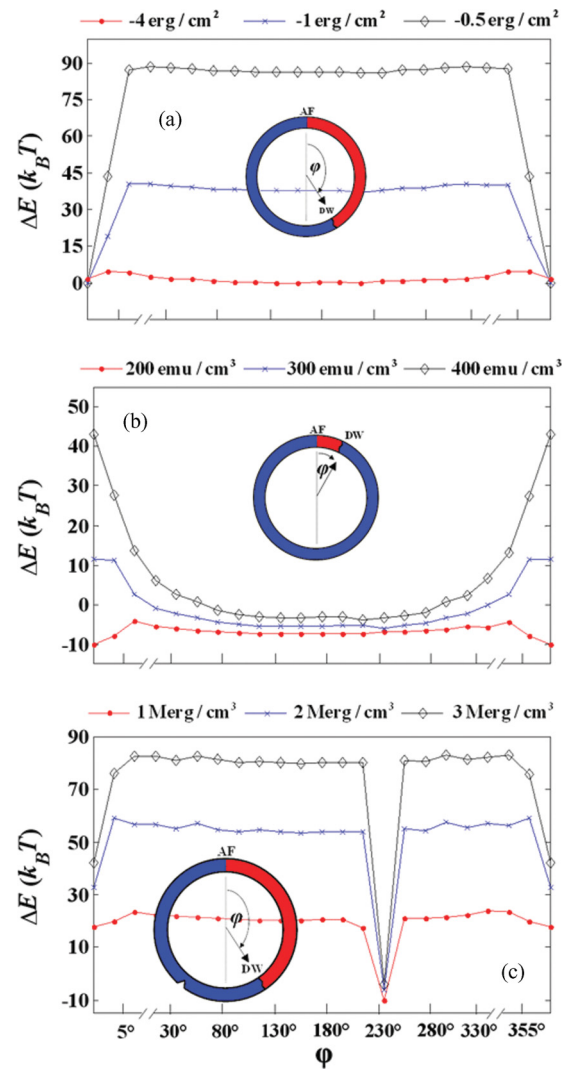


FIG. 3. (Color online) Energy landscapes for different MFNRs: energy as a function of DW location for three values of (a) AF coupling strength, $J_{AF} = -4, -1, \text{ and } -0.5 \text{ erg/cm}^2$; (b) saturation magnetization, $M_S = 200, 300, \text{ and } 400 \text{ emu/cm}^3$; and (c) magnetocrystalline anisotropy, $K_U = 1, 2, \text{ and } 3 \text{ Merg/cm}^3$. Remaining material parameters are in (a) $M_S = 225 \text{ emu/cm}^3$, $K_U = 1 \text{ Merg/cm}^3$; (b) $K_U = 1 \text{ erg/cm}^3$, $J_{AF} = -4 \text{ erg/cm}^2$; and (c) $M_S = 200 \text{ emu/cm}^3$, $J_{AF} = -4 \text{ erg/cm}^2$. The intralayer exchange constant, inner ring radius, outer ring radius, and ring thickness in all cases are $A_{ex} = 1.0 \mu\text{erg/cm}$, $R_{in} = 75 \text{ nm}$, $R_{out} = 90 \text{ nm}$, and $t = 12 \text{ nm}$, respectively. The notch depth in part (c) is 7.5 nm with about 65° notch angle. Energy landscapes have been offset for clarity (see discussion in text).

head-to-tail configuration. For the DW at the interface in the top image of Fig. 2(a), a large part of the energy is stored in bulk exchange (due to magnetization nonuniformity in the immediate vicinity of the interface) and anisotropy (due to magnetization deviation from the easy axis). However, upon closer inspection, the magnetization across the AF interface is found not perfectly antiparallel, due to competition between different energy terms. The total DW energy therefore includes an important interfacial exchange contribution. When the coupling strength $|J_{AF}|$ is large, even a small departure from

antiparallel alignment results in a large interfacial exchange energy. For reduced $|J_{AF}|$, the departure from antiparallel alignment at the AF interface is more prominent [Fig. 2(b)]. The MFNR material properties (M_S, K_U, J_{AF}) and geometry (inner and outer ring radius, thickness) offer freedom to tailor energy landscapes to be flat or include energy barriers or wells. For the case of flat energy landscapes, the MFNR can be viewed as a loop containing a single DW that can freely move in either direction throughout the nanoring. The closed loop prevents the DW from escaping the structure, which makes the MFNR particularly interesting for long-time studies of stochastic dynamics and DW propagation paths as a function of damping, temperature, DW width, and other parameters.^{16,17}

Before moving on to a discussion of Figs. 3(b) and 3(c), we mentioned that in our study of MFNRs we are primarily interested in the relative energy landscapes of each ring model which control the DW mobility, and need not consider common reference (or ground-state) energies. In all plots in Fig. 3 we, therefore, have translated the energy landscapes to be within a similar range for clarity. Figure 3(b) illustrates the effect magnetostatic interactions can have on the character of the energy landscapes in MFNRs. The ability to flatten the energy landscape via AF coupling depends on the sample magnetization M_S . For larger M_S the energy required to bring the DW to the AF interface can be very large [Fig. 3(b)]. As the DW approaches the interface, a region of unreversed magnetization [colored red in the inset of Fig. 3(b)] becomes increasingly confined between oppositely oriented segments of the ring, leading to dipolar interactions which can stabilize the magnetization configuration. This is similar to the stabilization of the antiparallel configuration of recorded bits in magnetic recording media due to closed flux lines. This effect leads to the upturn in the energy near the AF coupled region in Fig. 3(a). This barrier can be modulated by reducing the ring width near the AF interface to compensate the increase in magnetostatic energy with a decrease in anisotropy energy.

Extrema and saddle points can be further introduced to the energy landscape by adding artificial notches which trap the DW in an energy minimum.¹⁸ Edge roughness and intrinsic pinning sites may then introduce intrinsic distortion to the energy landscape, which can have an additional effect on magnetization dynamics and stability.⁵ Figure 3(c) shows the energy landscape for a magnetically frustrated ring containing one artificial notch located at an azimuthal angle of $\varphi_n = 235^\circ$ with respect to the perpendicular reference line (see inset). The notch spatially confines the DW so that its width (and hence energy) are reduced. The DW for the parameters used is a transverse DW. In the example of Fig. 3(c), a notch size was chosen that reduces the ring width by a factor of 2 at the notch center. This approximately lowers the DW width (the extent of the DW in the direction normal to the ring circumference at $\varphi_n = 235^\circ$), w_0 , by a factor of 2 as well. In a nanowire with a transverse DW and no notches, changes in anisotropy K_U result in the broadening (contracting) of the DW due to the competition between anisotropy energy, E_{anis} , and exchange energy, E_{ex} , which leads to the square root dependence of DW surface energy density on anisotropy energy density, as expressed in $\sigma_{DW} \approx 4\sqrt{K_U A_{ex}}$. However, in the presence of a notch [Fig. 3(c)], the physical constriction suppresses variations of the DW profile with a changing

K_U . With a fixed magnetization profile assumed, the DW energy is linearly proportional to anisotropy density, $E_{DW} = K_U \int (\hat{\mathbf{m}} \cdot \hat{\mathbf{k}})^2 dV + E_{ex}(\hat{\mathbf{m}})$, where $\hat{\mathbf{m}}$ is the magnetization unit vector, $\hat{\mathbf{k}}$ is the easy axis direction, and integration is over the span of the DW. Despite the crudeness of the fixed magnetization profile approximation, comparison of the pinning potentials of the notches ΔE in Fig. 3(c) for $K_U = 1, 2$, and 3 erg/cm^3 indicate indeed a linear dependence on K_U , at least for the parameter range and notch dimensions considered here. We also note that increasing the width w or thickness t of the nanoring, or increasing the dimensions of the notch to achieve a greater constriction, would also lead to a deepening of the pinning potential of the notch, similarly as increasing K_U .

III. MAGNETIZATION DYNAMICS

We now turn to magnetization dynamics and illustrate some of the consequences of magnetic frustration on the response on the nanoring to external stimuli. Figure 4 shows the z component of unit magnetization $m_z = \hat{\mathbf{z}} \cdot \mathbf{M}/M_S$ versus time (solid black line) in response to an alternating applied magnetic field $\mathbf{H}_a = \hat{\mathbf{z}} H_a(t)$ (dotted blue line) in a MFNR with PMA. Simulation parameters are listed in the caption. The initial configuration of the MFNR is a remanent state with a DW located at the AF interface. The alternating applied field, with rise and fall time $\tau_a = 0.5 \text{ ns}$, period $T_a = 150 \text{ ns}$, and maximum amplitude $|H_a| = 100 \text{ Oe}$, drives the DW from the AF interface along the ring until it extends an angle of 2π at which point the DW is back at the AF interface, now with the ring magnetization in the opposite direction. The DW dwells in this position until the applied field is reversed, upon which it again departs the AF interface and propagates around the ring once more, repeating the process for as long as the stimulus is applied.

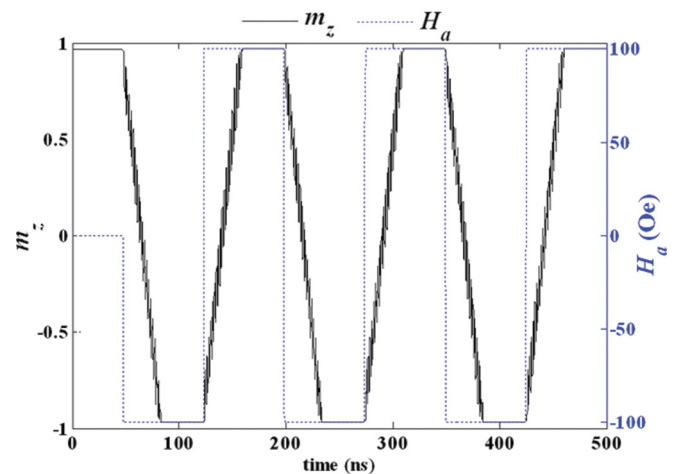


FIG. 4. (Color online) The z component of normalized magnetization (solid black line) of a MFNR under a vertically applied field (dashed blue line) as a function of time for a field switching period of $T = 150 \text{ ns}$. Simulation parameters are $M_S = 200 \text{ emu/cm}^3$, $K_U = 0.5 \text{ erg/cm}^3$, $J_{AF} = -1 \text{ erg/cm}^2$, and damping constant $\alpha = 0.1$. See end of caption to Fig. 3 for the remaining material and structural parameters.

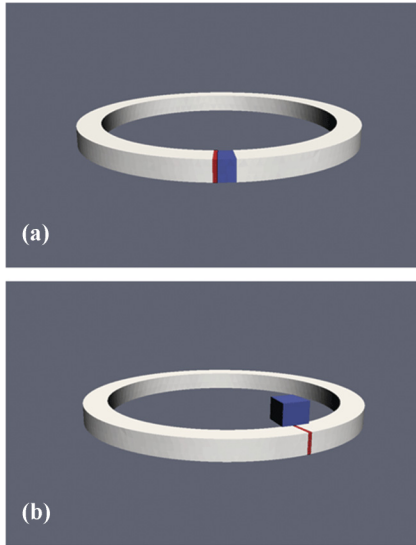


FIG. 5. (Color online) (a) MFNR with an irradiated (low anisotropy) region (colored blue) adjacent to the AF interface (red); (b) MFNR magnetostatically coupled to a magnetically soft nearby nanomagnet (blue).

Several important features should be pointed out. The field driving the DW motion is $|H_a| = 100$ Oe, which is 50 times smaller than the magnetocrystalline anisotropy field $H_{K_U} = 5$ kOe, and more than 30 times smaller than the coercive field $H_0 = 3.1$ kOe of a similar ring without AF coupling. Because the magnetic frustration necessitates the presence of a DW at all times, DW nucleation is not required. The DW driving field can be made, in principle, arbitrarily small by further tuning the system to obtain a more flat energy landscape. This is accomplished by tuning the system to yield equal energies when the DW is at the AF interface and away from it as in Fig. 3(a). When a large M_S is used, dipolar interactions can lead to a rise in energy when the DW is near the interface, as seen in Fig. 3(b). This can be compensated through magnetostatic coupling to a soft nearby nanomagnet [Fig. 5(b)], which orients itself with the applied field, counterbalancing the dipolar effect. Alternatively, tapering the ring near the AF interface would compensate the increase in magnetostatic energy by a decrease in anisotropy energy. We found that, for such configurations, operation is possible at much lower $|H_a|$ and considerably greater M_S .

It should be pointed out that the direction in which the DW departs the AF interface in an ideally symmetric MFNR and under a perfectly uniform applied field is arbitrary. The DW motion may be either in the clockwise (CW) or counterclockwise (CCW) direction during each revolution. A preferred cyclicity can be established by biasing the applied field to more strongly affect one side of the ring across the AF interface than the other. Alternatively, a segment of the ring adjacent to a chosen side of the AF interface can be tapered, or made slightly softer, e.g., by ion irradiation.¹⁹ Similarly, exchange coupling to a soft composite element may be utilized.²⁰ It is also possible to design a system with alternating or configurable cyclicity by employing exchange biasing²¹ and magnetostatics interactions with coupled or adjacent nanomagnets.²² The results in Fig. 4 were obtained for

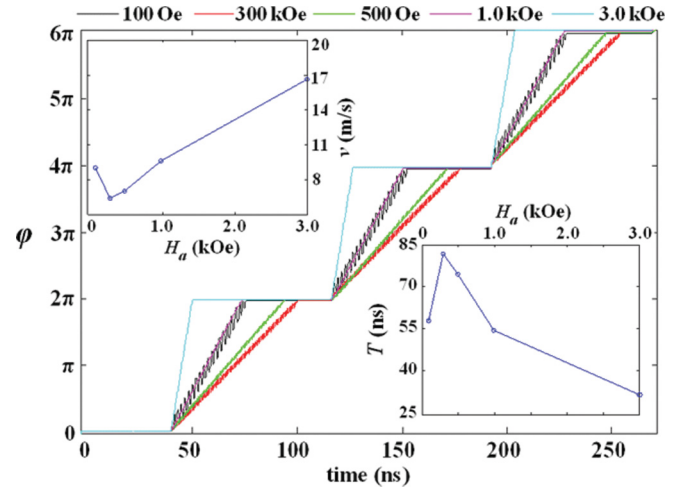


FIG. 6. (Color online) DW position given by angle φ (see Fig. 1) as a function of time for several values of applied field amplitude. The simulated MFNR and applied field frequency are the same as in Fig. 4. For all field amplitudes, the DW executes complete revolutions around the nanoring with the same cyclicity. The fluctuations in φ indicate DW propagation in the precessional regime. The mean DW velocity and revolution period as a function of field amplitude are given in the insets.

a nanoring with reduced anisotropy (10%) in a short segment immediately right to the AF interface, as illustrated in Fig. 5(a). Consequently, the DW motion was in the CW direction during the simulation (see Fig. 6).

Lastly, we note that the fluctuations in the vertical magnetization component m_z seen in Fig. 4 correspond to short intervals of backward motion of the DW during its advance forward. This phenomenon, known as Walker breakdown, is due to an instability of the DW structure under fields greater than the Walker threshold field H_W .

The time required for the DW to complete a full revolution can be varied by changing the strength and periodicity of the applied field. Figure 6 shows the azimuthal angle φ , relating the DW position [see Fig. 1(a)], versus time, for six alternating applied fields ranging in strength from 100 Oe to 3 kOe, having the same rise and fall times ($\tau_a = 0.5$ ns) and frequencies of switching ($f_a = 0.0067$ GHz) as in Fig. 4. The upper-left inset shows that the DW mobility dv_{DW}/dH_a is negative from 100 to 300 Oe, and positive for $H_a > 300$ Oe. The two regimes correspond to the nonlinear and linear precessional regimes, consistent with Walker theory.²³ A linear steady regime, expected for $H_a < H_W$ is not seen here since for our system H_W is low. Similarly, the bottom-right inset shows the time required for the DW to execute a full revolution for a given H_a . The frequency of revolution can therefore be tuned by adjusting the applied field intensity and period of switching. Modulating material and structural parameters can also serve to tailor DW mobility to access either the nonlinear or linear precession regime for a particular range of field amplitudes. Other recently proposed techniques for tuning DW mobility include the use of composites,²⁴ spin currents,²³ and comb²⁵ or wavy strips.²⁶

The range of distinct operation frequencies can be advantageous in terms of the performance of potential devices.

The fact that the DW upon reaching the AF interface is stationary until the applied field is reversed implies that a strict synchronization of field periodicity with the period of DW revolution is not mandatory for operation, and that a margin of error is tunable by adjusting the field frequency. The flat energy landscapes and closed-path geometry make MFRNs convenient for studies of stochastic behavior and propagation paths at long-time scales.^{16,17} In the case of MFNR spin valves or tunnel junctions with current perpendicular to plan (CPP), the effects of spin polarized currents on DW dynamics can also be investigated.²⁷ MFNR spin valves or magnetic tunnel junctions (MTJs) with CPP would be unique in that the high-conductivity channel would be a function of DW position, which itself would depend on the history of transmitted spin-current and applied magnetic fields. The cyclicity (digital) and DW position (analog) could be used as detectable logic outputs in potential magnetic circuits. For memory applications MFNRs with energy landscapes containing wells, at the least, $45 k_B T$ deep could be used for long-term stability, where k_B is the Boltzmann constant and $T = 300$ K. This implies the use of MFNRs with notches [Fig. 3(c)], or weak coupling at the AF interface [Fig. 3(a)].

IV. CONCLUSIONS

In summary, MFNRs possess several distinguishing features suggesting their usefulness for potential DW-based applications. As a result of magnetic frustration, only one mobile DW with an associated DW energy exists in the MFNR, as opposed to zero DWs or an even number of DWs that result in nonfrustrated rings. The DW in a MFNR is in permanent existence, can dwell anywhere along the ring, and can never escape or be annihilated by another DW. Another key feature is that the energy landscape can be made very flat with a proper choice of material and structural parameters. As a consequence, an alternating magnetic field with a very small magnitude can controllably drive the DW in consecutive circles around the ring. It was shown that a full range of operations are possible in a MFNR with low applied field magnitudes. It was also shown that MFNRs can be biased in order to set a specified cyclicity of DW motion to either CW or CCW. Energy landscapes with barriers and wells were demonstrated. The unique features of MFNRs can be found appealing for both logic and memory applications.

APPENDIX: MODELING

In the present work the MFNR is modeled as a homogeneous ferromagnetic material, with AF coupling at the $\varphi = 0$ interface (Fig. 1). The inner and outer radii of the ring are $R_{\text{in}} = 75$ nm and $R_{\text{out}} = 90$ nm, respectively, and the ring thickness is $t = 12$ nm. The AF interface consists of a 0.5 nm nonmagnetic interlayer or contact boundary separating two regions of magnetic material. The ring structure is discretized into tetrahedrons with a 4 nm mesh size using GID software.²⁸ The two surfaces on each side of the contact boundary are identically triangularized. Each node of the mesh is assigned a unit magnetic moment vector $\hat{\mathbf{m}}_i$ representing the magnetization direction at that point in space. The magnetization direction on the tetrahedral faces, and within the volume of

each tetrahedron, is interpolated linearly from the directions at the tetrahedral vertices, i.e., $\hat{\mathbf{m}} = \sum_{k=1}^4 \xi_k \hat{\mathbf{m}}_k$. Here, $\xi_k(\mathbf{r})$ is a hat basis function which equals unity at vertex k , linearly tapers off to zero at the opposite tetrahedral face, and is zero outside of the tetrahedron. The effective field at node i is given as a sum of Zeeman, magnetocrystalline anisotropy, magnetostatics, bulk exchange, and interfacial exchange fields, $\mathbf{H}_i^{\text{eff}} = \mathbf{H}_i^{\text{Zee}} + \mathbf{H}_i^{\text{anis}} + \mathbf{H}_i^{\text{ms}} + \mathbf{H}_i^{\text{ex}} + \mathbf{H}_i^{\text{ieX}}$. The expressions for the first four fields in the finite element linear basis representation are given in Ref. 29. We derive the (fifth) interfacial exchange field $\mathbf{H}_i^{\text{ieX}}$ starting from the interfacial exchange energy

$$E = \int_S J_{\text{ex}}(\mathbf{r}) \hat{\mathbf{m}}_+(\mathbf{r}) \cdot \hat{\mathbf{m}}_-(\mathbf{r}) dS, \quad (\text{A1})$$

where $J_{\text{ex}}(\mathbf{r})$ is the interfacial exchange energy density, $\hat{\mathbf{m}}_+(\mathbf{r})$ and $\hat{\mathbf{m}}_-(\mathbf{r})$ represent the magnetization directions on opposite sides of the interface, and the integration is over the contact surface S . The subscripts $+$ and $-$ indicating the side of the interface are arbitrary and interchangeable. In the discretized form expression (A1) can be written as

$$E = J_{\text{AF}} \sum_t \int_{S_t} \left(\sum_{k=1}^3 \hat{\mathbf{m}}_k^{t+} \xi_k^{t+} \right) \cdot \left(\sum_{k=1}^3 \hat{\mathbf{m}}_k^{t-} \xi_k^{t-} \right) dS_t, \quad (\text{A2})$$

where the integration over the contact surface has been broken up into integration over interfacial contact triangles t . The hat basis function associated with the tetrahedral vertex opposite to the interfacial surface triangle t vanishes at the interface, hence the sums in (A2) are over three interfacial vertices only. Constant interfacial energy density has been assumed $J_{\text{ex}}(\mathbf{r}) = J_{\text{AF}}$. The interfacial exchange field at node i is then obtained from a first-order variation of the energy with respect to $\hat{\mathbf{m}}_i$,

$$\begin{aligned} \mathbf{H}_i^{\text{ieX}} &= \frac{1}{M_S V_i^{\text{eff}}} \frac{\partial E}{\partial \hat{\mathbf{m}}_i} \\ &= \frac{J_{\text{AF}}}{M_S V_i^{\text{eff}}} \sum_t \int_{S_t} \xi_i^{t+} \left(\sum_{k=1}^3 \hat{\mathbf{m}}_k^{t-} \xi_k^{t-} \right) dS_t. \end{aligned} \quad (\text{A3})$$

Here i is a global index representing a node on one of the sides of the interface, while k is a local index representing one of the nodes of a given triangle t on the opposite side. The volume V_i^{eff} associated with the node i is obtained via the box method $V_i^{\text{eff}} = \sum_m \int_{\Omega_m} \xi_i^m dV = \frac{1}{4} \sum_m V_m$, where the sum is over all tetrahedrons m , which have node i as one of its vertices, V representing the volume of tetrahedron m , and M_S is the saturation magnetization of the MFNR. Equation (A3) can be rewritten as

$$\mathbf{H}_i^{\text{ex}} = \frac{J_{\text{AF}}}{M_S V_i^{\text{eff}}} \sum_t \sum_{k=1}^3 \hat{\mathbf{m}}_k^{t-} \int_{S_t} \xi_i^{t+} \xi_k^{t-} dS_t. \quad (\text{A4})$$

Using the identity $\int_S \xi_1^m \xi_2^n \xi_3^p dS = 2m!n!p!/(2+m+n+p)!S$,³⁰ where ξ_1, ξ_2, ξ_3 are the three linear basis functions of a single triangle of area S , and m, n, p are exponents, we have

$$\mathbf{H}_i^{\text{ex}} = \frac{J_{\text{AF}}}{M_S V_i^{\text{eff}}} \sum_t \frac{S_t}{12} \sum_{k=1}^3 (1 + \delta_{ik}) \hat{\mathbf{m}}_k^{t-}. \quad (\text{A5})$$

Here S_t is the area of triangle t , and δ_{ik} is the Kronecker delta. If the mesh size is sufficiently smaller than the exchange

and domain wall length, Eq. (A5) can be approximated by $\mathbf{H}_i^{\text{ex}} = (J_{\text{AF}}/M_S t_i^{\text{eff}}) \hat{\mathbf{m}}_j^t$, where j represents the node opposite to node i across the AF interface, and $t_i^{\text{eff}} = S_i^{\text{eff}}/V_i^{\text{eff}}$, where $S_i^{\text{eff}} = \sum_t \int_{S_t} \xi_i^{t+} dS = \frac{1}{3} \sum_t S_t$. This approximation has the form of the interfacial exchange field often quoted in literature for multilayer films.³¹ However, Eq. (A3) gives the exact expression in the linear basis representation, and due to its low implementational complexity, does not require further simplification.

With the effective field $\mathbf{H}_i^{\text{eff}}$ known, magnetization dynamics can be simulated by integrating the Landau-Lifshitz-Gilbert (LLG) equation

$$\frac{d\hat{\mathbf{m}}_i}{dt} = -\frac{\gamma}{1+\alpha^2} \hat{\mathbf{m}}_i \times \mathbf{H}_i^{\text{eff}} - \frac{\alpha}{1+\alpha^2} \hat{\mathbf{m}}_i \times \dot{\hat{\mathbf{m}}}_i \times \mathbf{H}_i^{\text{eff}}, \quad (\text{A6})$$

where γ , α , t are the gyromagnetic ratio, damping constant of the material, and time, respectively. The numerical integration of the LLG equation proceeds as outlined in Ref. 29.

Calculation of the energy landscapes is performed using the nudged elastic band method (NEBM). This method consists

of integrating

$$\frac{d\hat{\mathbf{m}}^k}{d\tau} = -[\nabla_{\hat{\mathbf{m}}} E(\hat{\mathbf{m}})|_{\hat{\mathbf{m}}^k} - (\nabla_{\hat{\mathbf{m}}} E(\hat{\mathbf{m}})|_{\hat{\mathbf{m}}^k} \cdot \mathbf{t}^k) \mathbf{t}^k] \quad (\text{A7})$$

to the point when $\hat{\mathbf{m}}^k$ is considered to have converged, i.e., $\max(|d\hat{\mathbf{m}}^k/d\tau|) < \varepsilon$, where ε is the stopping parameter, usually around 10^{-4} – 10^{-6} , and τ is the arbitrary integration variable. Here, $\hat{\mathbf{m}}^k$ represents a composite vector of unit magnetization vectors $\hat{\mathbf{m}}_i^k$ at all nodes $i \in [1, N]$ of image $k \in [1, M]$, so that $\hat{\mathbf{m}}^k = [\hat{\mathbf{m}}_1^k \hat{\mathbf{m}}_2^k \cdots \hat{\mathbf{m}}_N^k]^T$, and the $\max()$ function used for the stopping criteria is with respect to the spatial components of all the elements. Each image k represents a magnetization configuration at a given point on the discretized transition path connecting two magnetization states. Typically 10–20 images are sufficient to resolve the transition between the two states. In (A7) $E(\hat{\mathbf{m}})$ is the energy functional of the system, and \mathbf{t}^k denotes the unit tangent along the path at image k , for $k \in [2, M-1]$, and is zero otherwise. It can be seen that the convergence of $\hat{\mathbf{m}}^k$ implies that the path is parallel to the energy gradient of the system. Details of the NEBM and the evaluation of the energy gradient lines can be found in Ref. 15.

¹J. G. Zhu, Y. F. Zheng, and G. A. Prinz, *J. Appl. Phys.* **87**, 6668 (2000).

²S. P. Li, D. Peyrade, M. Natali, A. Lebib, Y. Chen, U. Ebels, L. D. Buda, and K. Ounadjela, *Phys. Rev. Lett.* **86**, 1102 (2001).

³C. A. Ross, F. J. Castaño, D. Morecroft, W. Jung, Henry I. Smith, T. A. Moore, T. J. Hayward, J. A. C. Bland, T. J. Bromwich, and A. K. Petford-Long, *J. Appl. Phys.* **99**, 08S501 (2006).

⁴C. A. F. Vaz *et al.*, *J. Phys.: Condens. Matter* **19**, 255207 (2007).

⁵M. Klaui, C. A. F. Vaz, L. Lopez-Diaz, and J. A. C. Bland, *J. Phys.: Condens. Matter* **15**, R985 (2003).

⁶C. A. Ross, F. J. Castaño, W. Jung, B. G. Ng, I. A. Colin, and D. Morecroft, *J. Phys. D: Appl. Phys.* **41**, 113002 (2008).

⁷G. D. Chaves-O'Flynn, A. D. Kent, and D. L. Stein, *Phys. Rev. B* **79**, 184421 (2009).

⁸A. Imre *et al.*, *4th IEEE Conference on Nanotechnology*, IEEE Cat. No. 04TH8757 (IEEE, New York, 2004).

⁹D. A. Allwood, G. Xiong, C. C. Faulkner, D. Atkinson, D. Petit, and R. P. Cowburn, *Science* **309**, 1688 (2005).

¹⁰S. R. Bowden and U. J. Gibson, *IEEE Trans. Magn.* **45**, 5326 (2009).

¹¹D. T. Pierce, J. Unguris, R. J. Celotta, and M. D. Stiles, *J. Magn. Magn. Mater.* **200**, 290 (1999).

¹²A. Moser, A. Berger, D. T. Margulies, and E. E. Fullerton, *Phys. Rev. Lett.* **91**, 097203 (2003).

¹³J. E. Greedan, *J. Mater. Chem.* **11**, 37 (2001).

¹⁴O. Cador *et al.*, *Angew. Chem., Int. Ed.* **43**, 5196 (2004).

¹⁵R. Dittrich, T. Schrefl, D. Suess, W. Scholz, H. Forster, and J. Fidler, *J. Magn. Magn. Mater.* **250**, L12 (2002).

¹⁶D. Ravelosona, in *Dynamics of Domain Wall Motion in Wires with Perpendicular Anisotropy*, edited by J. P. Liu *et al.*, Nanoscale Magnetic Materials and Applications, 1st ed. (Springer, New York, 2009).

¹⁷M. Klaui, J. Rothman, L. Lopez-Diaz, C. A. F. Vaz, J. A. C. Bland, and Z. Cu, *Appl. Phys. Lett.* **78**, 3268 (2001).

¹⁸C. Burrowes *et al.*, *Nat. Phys.* **6**, 17 (2010).

¹⁹C. Chappert *et al.*, *Science* **280**, 1919 (1998).

²⁰D. Suess, T. Schrefl, S. Fähler, M. Kirschner, G. Hrkac, F. Dorfbauer, and J. Fidler, *Appl. Phys. Lett.* **87**, 012504 (2005).

²¹W. Jung, F. J. Castaño, D. Morecroft, C. A. Ross, R. Menon, and H. I. Smith, *J. Appl. Phys.* **97**, 10K113 (2005).

²²S. Jain and A. O. Adeyeye, *Europhys. Lett.* **84**, 17002 (2008).

²³A. Mougou, M. Cormier, J. P. Adam, P. J. Metaxas, and J. Ferré, *Europhys. Lett.* **78**, 57007 (2007).

²⁴J. Y. Lee, K. S. Lee, and S. K. Kim, *Appl. Phys. Lett.* **91**, 122513 (2007).

²⁵E. R. Lewis, D. Petit, L. O'Brien, A. Fernandez-Pacheco, J. Sampaio, A.-V. Jausovec, H. T. Zeng, D. E. Read, and R. P. Cowburn, *Nat. Mater.* **9**, 980 (2010).

²⁶H. G. Piao, J.-H. Shim, S.-H. Lee, D. Djuhana, S.-K. Oh, S.-C. Yu, and D.-H. Kim, *IEEE Trans. Magn.* **45**, 3926 (2009).

²⁷C. Burrowes, D. Ravelosona, C. Chappert, S. Mangin, E. E. Fullerton, J. A. Katine, and B. D. Terris, *Appl. Phys. Lett.* **93**, 172513 (2008).

²⁸GID software, available at <http://gid.cimne.upc.es>.

²⁹R. Chang, S. Li, M. V. Lubarda, B. Livshitz, and V. Lomakin, *J. Appl. Phys.* **109**, 07D358 (2011).

³⁰A. F. Peterson, S. L. Ray, and R. Mittra, *Computational Methods for Electromagnetics* (Oxford University Press/IEEE Press, Oxford/New York, 1998).

³¹R. C. O'Handley, *Modern Magnetic Materials: Principles and Applications* (Wiley, New York, 1999).